Wavelength-dependence of photoelectron spectra in above-threshold ionization.

T Marchenko[1,2,3], H G Muller[1], K J Schafer[4] and M J J Vrakking[1,5]

[1] FOM Institute for Atomic and Molecular Physics (AMOLF), Science Park 113, 1098XG Amsterdam, The Netherlands
[2] Laboratoire de Chimie Physique-Matière et Rayonnement, UMR 7614 UPMC Univ Paris 6-CNRS, 11 rue Pierre et Marie Curie, F-75005 Paris, France
[3] Laboratoire d'Optique Appliquée, UMR 7639 CNRS-ENSTA-Ecole Polytechnique, Chemin de la Hunière, F-91761 Palaiseau, France
[4] Department of Physics and Astronomy, Louisiana State University, Baton Rouge, Louisiana 70803-4001, USA
[5] Max-Born-Institut, Max Born Straße 2A, D-12489 Berlin, Germany

E-mail: tatiana.marchenko@upmc.fr

Abstract

We present angle- and energy-resolved measurements of photoelectrons produced in strong-field ionization of Xe and Ar using a tunable femtosecond laser in the wavelength range between 600 and 800 nm. Systematic analysis of the experimental data that are quantitatively reproduced by numerical solutions of the time-dependent Schrödinger equation with integration over the laser focal volume, demonstrates the dominance of resonance-enhanced ionization. Continuous variation of the laser wavelength allows the identification of a number of consecutive channel-switching effects with a reliable assignment of the intermediate Rydberg states involved. The appearance of the resonant sub-structure in the electron energy spectra is influenced by the presence of a non-resonant contribution. At relatively low laser intensity a coherent addition of resonant and non-resonant ionization processes is observed. Due to the absence of an intensity dependence in the resonance-enhanced ionization, we observe the persistence of Freeman resonances at the transition to the tunnelling regime.

(Some figures in this article are in colour only in the electronic version)

1. Introduction.

The discovery of above-threshold ionization (ATI) in 1979 [1] was the first experimental manifestation of a non-perturbative strong-field light-matter interaction: at sufficiently high laser intensity an atom was shown to absorb photons in excess of the minimum number needed to reach the ionization threshold, resulting in a photoelectron energy spectrum (PES) containing peaks separated by the photon energy. In the short-pulse regime (i.e. when the duration of the ionizing laser pulse τ_{pulse}

is shorter than the time it takes a photoelectron to leave the interaction volume, typically τ_{pulse} < 1ps) the absolute position of ATI peaks in the PES depends on the value of the ponderomotive energy U_p [2] and therefore on the laser intensity I_{laser}:

$$E_{non-resonant} = (n+s)\omega - (IP + U_p) \qquad (1)$$

$$U_p = I_{laser} / 4\omega^2 = A_{\max}^2 / 4 \qquad (2)$$

where n is the minimum number of photons with energy ω necessary to overcome the ionization potential IP, and s=0,1,2… is the number of photons absorbed by the atom above the ionization threshold and consequently the number of the ATI order. I_{laser} is the peak intensity of the laser pulse, A_{max} is the maximum of the vector potential. In our discussion, atomic units ($e=m_e=\hbar=1$) are used throughout, unless mentioned otherwise.

Resonant population of ac-Stark shifted Rydberg levels of an atom with an integer number of laser photons leads to resonant enhancement of the ionization yield, and results in the appearance of sub-structures within the low-energy ATI peaks, known as Freeman resonances [3]. Since high-lying Rydberg levels experience ponderomotive shifts that are very similar to the ponderomotive shift of the ionization continuum, the position of these resonant features in the PES is independent of the temporal and spatial profile of the laser pulse (including the peak laser intensity) and depends only on the photon energy and the number of photons absorbed:

$$E_{resonant} = n\omega + E_b \qquad (3)$$

where E_b is the binding energy of the respective Rydberg level and n will generally be a low number. Simultaneous measurements of electron energy and angular distributions enabled by photoelectron imaging techniques [4, 5, 6, 7, 8] and a careful quantitative comparison of experimental electron-momentum distributions with theoretical volume-integrated spectra allowed the identification of processes like channel switching, i.e. a change in the number of photons required for resonant population of a Rydberg series upon increase of the laser intensity, as well as multi-photon resonant and non-resonant ionization, and ac Stark splitting [9].

Measurement of photoelectron spectra at a number of laser intensities and at a fixed wavelength (usually 800 nm) are commonly used in ATI studies. However, the limited range of experimentally available intensities restricts the observed phenomena to a relatively narrow set of parameters. Measurements of *wavelength-dependent* ATI PES present an attractive alternative. Varying the laser wavelength between 592 and 616 nm and measuring photoelectron energy and angular distributions, Rottke et al. [10] observed channel switching from 6- to 7-photon resonant ionization in Xe. Continuous variation of the laser frequency in Xe ATI photoelectron energy measurements was performed by Kaminski et al. [11] in the range of wavelengths between 500 and

650 nm and at intensities between 10^{12} and 10^{13} W/cm^2. Measuring photoelectron energy and angular distributions as a function of the ionizing wavelength allowed the authors to observe the transition between resonant and non-resonant ionization channels and to identify the excited states involved in the ionization process.

Well-resolved peak structures are predicted in ATI PES when strong-field laser ionization is explained in terms of the multiphoton ionization mechanism, defined by the condition that the Keldysh parameter $\gamma = (IP/2U_p)^{1/2} > 1$. Conversely, in the tunnelling regime, where the peak laser intensity is high ($\gamma<1$), one might expect the ATI peak structure to be completely washed out due to the fact that all laser intensities below the peak laser intensity are present in the focal volume and contribute to ionization. However, recent experiments have demonstrated the persistence of ATI structures into the tunnelling regime. Two-dimensional photoelectron momentum spectra measured by Rudenko et al. [12] in the tunnelling regime in He, Ne and Ar unexpectedly demonstrated complex structures within the first few ATI orders, characterised by highly oscillatory angular distributions. Similar structures were observed by Maharjan et al. [13] for Ar at selected wavelengths in the range from 400 to 800 nm for $\gamma<1$. Very recent theoretical studies confirm the importance of the discrete photo-absorption even deep in the tunneling regime. Two-dimensional photoelectron spectra calculated in He at $\gamma=0.58$ reveal ATI-like rings similar to the ones observed in [12, 13] with nodal structures sensitive to the laser intensity and the photon frequency [14]. Furthermore, Potvliege et al [15] explored the importance of the resonant coupling of the field with intermediate excited states in the tunneling regime and predicted that at $\gamma<1$ ionization from the ground state can still be significantly affected by multiphoton resonances.

In this paper we present experimental and theoretical results on ATI in Xe and Ar over a wide range of parameters. Choosing an adequate wavelength step we track the smooth continuous evolution of the two-dimensional ATI photoelectron momentum spectra as a function of the laser wavelength from 600 to 800 nm. We identify a number of consecutive channel-switching effects upon continuous variation of the laser wavelength. Inspection of the electron kinetic energy spectra and the angular distributions of the resonantly ionized electrons allows us to reliably assign the intermediate Rydberg states involved in the ionization process. Our experimental results are supported by good quantitative agreement with results of calculations solving the time-dependent Schrödinger Equation (TDSE). These calculations were performed with full integration over the laser focus volume. We discuss the possibility of simultaneously observing structures in the PES arising from both direct non-resonant ATI from the ground state and resonance-enhanced ionization via intermediate Rydberg states in the multiphoton regime and the persistence of the resonant features at the transition to the tunnelling regime in agreement with the earlier experiments [12, 13].

2. Experimental and theoretical methods.

In the experiment, a commercial laser system consisting of an optical parametric amplifier (OPA, *Coherent Opera*) pumped by 1 mJ from a 1 kHz Ti:Sapphire amplifier system (800 nm, 50 fs) was used. The OPA signal output was frequency-doubled using a BBO crystal, providing pulses with a wavelength in the range from 600 to 800 nm with a FWHM of 10-15 nm. The central wavelength was determined with an accuracy of 2 nm using a spectrometer. The linearly polarized laser beam was focused onto a pulsed atomic beam (25 Hz) using a spherical normal-incidence silver mirror (f=75 mm). The ejected electrons were detected using a Velocity Map Imaging (VMI) spectrometer [16], consisting of a set of acceleration electrodes, a flight tube, a dual MCP and a phosphor screen. Images were recorded using a computer-controlled CCD camera. Retrieval of the velocity and angular distribution of the measured photoelectrons was performed by using an iterative procedure of inverse Abel transform [[17]]. Slices through the 3D velocity and angular distribution of the ionized electrons are referred to in the following as momentum maps.

In order to explore the evolution of the momentum spectra with the laser wavelength photoelectron momentum maps were recorded in Xe and Ar over a range of wavelengths between 600 and 800 nm while attempting to keep the laser intensity constant using the ratio of double-to-single ionization as a rough indicator. In the analysis the experimental intensity was deduced by comparing the measured results to numerical solutions of the 3D TDSE within the single-active electron (SAE) approximation [18], i.e. considering only the response of the outermost valence electron to the laser field. In order to solve the TDSE for Xe we used a code based on the method outlined in [19, 20] with a pseudo-potential described in [21]. The TDSE for Ar was solved using the numerical algorithm described in [22]. Application of this algorithm for calculations of ATI spectra in a model Ar atom was previously demonstrated in [23]. Both codes provide energy-resolved electron angular distributions, which can be converted into a 2D momentum map that allows comparison with the experimentally recorded images. For an adequate comparison to the experiment the results of the TDSE calculations were integrated over the laser focal volume using the prescription described in [24], assuming a Gaussian focus in an infinitely extended medium. The temporal profile of the laser pulse was modelled with a sine-squared envelope typically containing 60 optical cycles.

3. Argon results

Figure 1 shows a series of momentum maps at wavelengths between 600 and 800 nm, where experimental images presented on the left are compared to TDSE results on the right. The vertical and horizontal axes in Figure 1 show the electron momenta in a range from –1 to 1 a.u. parallel and perpendicular to the laser polarisation axis, respectively. This momentum scale corresponds to electron kinetic energies up to 13.6 eV. The calculations are simulations of the experiment including full 3D volume averaging, assuming a laser focus with a peak intensity I_0 corresponding to a value of the vector potential $A_{max} = (I_0/\omega^2)^{1/2} = F_0/\omega$, where F_0 is the amplitude of the laser field. The peak laser intensity used in the calculations was chosen to provide the best agreement with the experimental data

(based on visual inspection) and remained on average around 1.2×10^{14} W/cm^2 with an estimated error of less than 5% in the individual intensities.

Several contributions can be distinguished in the electron momentum spectra presented in Figure 1. The most prominent contribution peaks along the laser polarisation axis and consists of a series of relatively broad features that correspond to direct non-resonant ATI from the ground state (see below). Within the broad ATI features narrow sub-structures can be observed, that are identified as Freeman resonances, and that are characterised by highly oscillatory angular distributions. Below the first ATI order the momentum maps contain cross-like radial patterns fanning out from the centre of the image, which were discussed in detail in our recent paper [25]. In addition, a weak off-axis pattern can be observed on the periphery of the momentum maps, which we believe to be due to the interference of electrons that are launched at different times within the optical cycle. These off-axis patterns are the subject of a future publication [26]. Here we will concentrate on the analysis of the contributions from non-resonant ATI and resonance-enhanced ionization, which appear to be dominant in the considered experimental regime.

For an overview of our experimental results it is convenient to present the angle-integrated photoelectron kinetic energy spectra in a contour plot as a function of the laser frequency (Figure 2). Individual energy distributions were normalised so that $\int P(E)dE=1$. The probability for a photoelectron to be ionized with a given kinetic energy at a given laser frequency is coded on a logarithmic colour scale, which covers one order of magnitude. Monitoring the kinetic energy of a particular non-resonant or resonant feature in the photoelectron spectra as a function of the laser frequency one can obtain a linear dependence according to Eqns. (1) and (3), respectively, with a slope corresponding to the number of photons involved in the ionization process. In the case of non-resonant ionization the linear frequency dependence is only possible under the condition of constant value of the ponderomotive energy U_p. A set of continuous branches can be observed in Figure 2**.** Black dotted lines were calculated according to Eqn. (3), where E_b= -0.85 eV and n varies from 1 to 5, indicating low-order ionization processes involving the population of intermediate resonant states. The contour plot contains no sign of branches, which could be attributed to high-order non-resonant processes given by Eqn. (1).

To facilitate identification of the intermediate resonant states involved in the low-order ionization processes, Figure 3 shows the experimental and calculated PES downshifted by the energy of one photon at a number of laser wavelengths relevant to Figure 1. As a result of this procedure suggested by Maharjan et al. [13], the position of a peak corresponding to a particular resonance becomes independent of the wavelength and corresponds to the binding energy of this resonance. In order to suppress the contributions from non-resonant ionization, the PES presented in Figure 3 were integrated beyond an angle of ±25 degrees from the laser polarisation axis. In the case of non-resonant ionization, the electron is removed from the ground state of the atom by the absorption of many laser photons. Therefore the angular distribution of the photoionized electron is strongly aligned along the

polarisation axis. On the other hand, electrons that are first excited to an intermediate Rydberg level and that are subsequently ionized by means of a low-order process, are expected to have an angular distribution that reflects the orbital angular momentum of the Rydberg state, generally implying a significant off-axis component. Similar to figure 2, the spectra presented in Figure 3 are normalised so that $\int P(E)dE=1$ and are plotted on a common scale.

Assignment of the resonant states was performed in the following way: the binding energy corresponding to a peak observed in the spectrum was compared to the NIST atomic database (http://physics.nist.gov/PhysRefData/ASD/index.html), which allowed identification of the principal quantum number of the contributing Rydberg state. However, for states with a high orbital angular momentum the quantum defect is negligible, so that a peak at a given binding energy can be attributed to different angular momentum states with the same principal quantum number. A unique assignment of the peaks observed in the PES requires inspection of the angular distributions. Figure 4 shows experimental and calculated angular distributions of the photoelectrons appearing in the PES within the first ATI order at the position of the peaks attributed to ionization via 4*l*, 5*l* and 6*l* Rydberg states, where *l* is the orbital angular momentum of the particular resonant state.

At 800 nm peaks in the spectrum are observable at binding energies of -0.6 and -0.4 eV. According to the Rydberg formula this corresponds to 5*l* and 6*l* resonances with high orbital angular momentum *l*, which are expected at -0.55 and -0.38 eV, respectively. The estimated intensity at 800 nm is 0.82×10^{14} W/cm^2. If ionization were to occur at this intensity it would require at least 14 photons in order to overcome the ponderomotively shifted ionization threshold. Consequently, resonant population of the Rydberg states should have involved 13 photons. However, resonant population of a 5*l* state with 13 photons at 800 nm requires an intensity equal to 0.83×10^{14} W/cm^2, which is just above the peak laser intensity in the experiment. Therefore the peaks in the spectrum are expected to be due to 12-photon resonant ionization. As required by the parity selection rules ionization should then proceed via states with odd orbital angular momentum. At 800 nm the angular distributions for the 5*l* and 6*l* resonant states (Figure 4) contain 6 minima between 0 and 180 degrees, suggesting 5*f*, 6*f* (*l*=3) and 6*h* (*l*=5) as the corresponding resonant states. Our present measurement can be compared to the results of Wiehle et al. [9], where a detailed comparison between the experiment and the calculated photoelectron momentum spectra at 800 nm and at various intensities was performed. Wiehle et al. attributed the structure observed in the spectrum obtained at 0.7×10^{14} W/cm^2 to 12-photon resonant ionization via 4*f* and 5*p* states. In our case the spectrum acquired at 0.82×10^{14} W/cm^2 contains contributions from 12-photon resonant ionization via 5*f* and 6*f*/6*h* states, whereas a possible contribution from the 5*p* state is completely hidden under the non-resonant contribution.

Resonant (12+1)-photon ionization with involvement of the *f*- and *h*-series continues to dominate the spectra for the wavelengths down to 750 nm. At still shorter wavelengths (11+1)-photon resonant ionization via the *g*-series becomes dominant. At 700 nm 11-photon resonant ionization via

the 5*g* state requires an intensity of 0.93×10^{14} W/cm^2, which is close to the peak laser intensity in the experiment, which is estimated as 1.15×10^{14} W/cm^2. Channel switching from ionization via the 5*f* and 6*f*/6*h* states at 750 nm to ionization via the 5*g* and 6*g* states at 700 nm is indicated by the change in the corresponding angular distributions from 6 to 5 minima between 0 and 180 degrees in Figure 4. A peak appearing in the spectrum at 700 nm at a binding energy around -0.9 eV can be attributed to (10+1)-photon resonant ionization via the 4*f* state consistent with 4 minima in the angular distribution in Figure 4. The relative importance of the 4*f* resonance grows upon further decrease of the laser wavelength down to 650 nm. At this wavelength the 5*g* resonance is just on the edge of the appearance threshold, since as the laser wavelength decreases, the intensity where a given state shifts into resonance increases. At 650 nm the laser intensity required in order to shift the 5*g* state into resonance with 11 photons equals the peak laser intensity (1.5×10^{14} W/cm^2). At the same time the resonant population of the 4*f* state (and higher *f*- and *h*-states) with 10 photons still remains possible in the laser focus volume leading to the dominance of the 4*f* state in the spectrum. Assignment of the peaks as *f*- and *h*-states is confirmed by the presence of 6 minima in the calculated angular distributions. Due to a limited experimental resolution we observed only 4 minima in the angular distributions at 650 nm, which is still consistent with assignment of *f*- and *h*-states. At the short-wavelength end of our measurements, the (9+1)-photon channel becomes responsible for the appearance of the *g*-series in the spectra, while the (8+1)-photon channel leads to the peak attributed to the 4*f* state. Consequently, at 600 nm and a laser peak intensity of 1.23×10^{14} W/cm^2 the angular distributions corresponding to the 5*l* and 6*l* show 5 minima in agreement with one-photon ionization from the *g*-states.

To summarise, the evolution of the resonant ionization channel with the laser wavelength in the range from 600 to 800 nm in Ar demonstrates a number of channel-switching effects – from 12-photon resonant ionization at 800 nm to 8-photon resonant ionization at 600 nm.

4. Xenon results

Figure 5 presents a series of momentum maps for Xe at several wavelengths between 600 and 800 nm. In these measurements the intensities used were on average $4\text{-}7\times10^{13}$ W/cm^2 as follows from a comparison with TDSE results shown to the right of the experimental data. Analysis of the Xe electron spectra was performed in analogous manner as was previously done for the case of Ar. In order to avoid repetition we skip the details of the data treatment procedure and provide only a short summary of the analysis. In this section we focus on the coincident occurrence of resonant and non-resonant contributions and discuss their relative manifestation with increasing laser intensity.

The evolution of the dominant resonant ionization channel in the considered wavelength range demonstrates a number of occurrences of channel switching from 9-photon resonant ionization via 5/6/7*g*-states at 800 nm, through 8-photon resonant ionization via 4*f*- and 6/7*h*-states around 730 nm, through 7-photon resonant ionization via 5/6/7*g*-states between 700 and 640 nm, to – finally – 6-

photon resonant ionization via 4/5/6*f*-states at the short-wavelength end of our measurements close to 600 nm. In addition to the dominant resonant contribution the Xe data demonstrate a strong presence of non-resonant ionization. Here we exploit the capacity provided by TDSE calculations, where control over the laser intensity provides the possibility to monitor the non-resonant, strongly intensity-dependent ionization, its evolution with the laser wavelength and interaction with the resonant contributions in the electron spectra. According to Eqn. (1), the photoelectron kinetic energy in a non-resonant ionization process depends on the laser intensity through the ponderomotive energy Eqn. (2). We choose to explore the wavelength-dependence of the calculated ATI spectra at a constant value of the maximum ponderomotive energy in the laser pulse, which provides a linear dependence of the electron kinetic energy on the laser frequency and therefore facilitates the comparison with the resonant contribution. In the following calculations we choose U_p=2.45 eV, which corresponds to a maximum of the vector potential A_{max}=0.6 a.u. and a Keldysh parameter γ=1.57, indicating the multiphoton regime. At this value of the vector potential both resonant and non-resonant contributions have comparable importance and can be simultaneously observed in the fully angle-integrated photoelectron spectra obtained in TDSE calculations (Figure 6a). The photoelectron spectra presented in Figure 6a are integrated over the laser focal volume and plotted in a contour plot as a function of the laser wavelength. Two sets of branches observable in the contour plot can be fitted according to Eqns. (1) and (3) with slopes corresponding to high-order (n=11, 12, 13 photons, solid lines) and low-order (n=1, 2, 3 photons, dotted lines) ionization processes for non-resonant and resonant ionization, respectively.

Knowing the laser intensity we can determine the position of the non-resonant ATI peaks in the PES. However, closer inspection of the calculated PES shows that the position of the non-resonant branches cannot be directly related to the value of the maximum of vector potential used in the calculations, since the ponderomotive shift induced by the laser is not exclusively determined by the peak laser intensity, but depends to a large extent on the presence of slightly lower intensities in the laser focal volume. The range of intensities contributing to the ponderomotive shift of the ionization threshold determines the width of the non-resonant branches. In order to establish the value of the "effective" intensity responsible for the position of the non-resonant branches, we need to evaluate the relative weight of all the intensities that are present in the laser focus, as given by the product of the intensity-dependent energy-integrated ionization yield and the intensity-dependent laser volume element:

$$P(I) = \int_E P_I(E) dE \frac{\partial V}{\partial I} dI , \qquad I \le I_0$$

where I_0 is the peak intensity in the laser focal volume and $\frac{\partial V}{\partial I} dI$ is the volume element experiencing an intensity between I and $I+dI$. Here it is implicitly assumed that the main effect of a small-intensity

shift is the corresponding ponderomotive shift of the photoelectron spectrum. This is an approximation, as the photoelectron spectrum not only shifts but also changes shape when the intensity is changed. The solid lines marking the position of the non-resonant branches in Figure 6a are plotted according to Eqns. (1) and (2), using the calculated "effective" value of the vector potential A_{eff} = 0.53 a.u. The widths of the branches are determined by intensities in the focal volume corresponding to $0.45<A<A_{max}=0.6$ a.u and are shown with dashed lines.

As we can observe in Figure 6a the non-resonant contribution competes with the resonant contribution at this relatively low value of the vector potential. Furthermore, it has an effect on the appearance of the resonant sub-structure in the contour plot. The resonant sub-structure is most prominent whenever it overlaps with a non-resonant branch. For example, at the laser frequency of 0.061 a.u., resonant sub-structures are very prominent within the first ATI order around a kinetic energy of 1 eV. Remarkably, the first-order resonant ionization branch crosses over at this laser frequency and kinetic energy with a 9-photon non-resonant ionization branch. In contrast, at a laser frequency of 0.066 a.u. the resonant sub-structures are hardly observable within the first order due to the absence of non-resonant ionization. In other words, at a relatively low intensity we can observe the coherent addition of resonant and non-resonant ionization processes and a resulting modulation of the intensity of the resonant sub-structure. Nevertheless, resonant sub-structures can be well resolved on top of the non-resonant contributions.

Further increase of the peak laser intensity enlarges the range of intensities in the focal volume. The corresponding range of ponderomotive shifts increases accordingly and may substantially exceed the photon energy in our wavelength range. Therefore any intensity dependent non-resonant features no longer appear in the photoelectron spectra as regular structures but are completely washed out due to the focal volume integration. Figure 6b shows the focal volume averaged PES as a function of the laser frequency at a constant value of the ponderomotive energy U_p=5.5eV, which corresponds to a maximum of the vector potential A_{max}=0.9 a.u. and the Keldysh parameter γ=1.05, i.e. around the transition to the tunnelling regime. Under these conditions the ponderomotive shift exceeds the photon energy by more than a factor two. Branches observable in the contour plot can be fitted with slopes corresponding to low-order (n=1, 2, 3 photons) ionization processes, indicating resonant ionization. As expected at this high value of the ponderomotive energy no signature of non-resonant structure can be observed. On the other hand, intensity independent resonant features become even more prominent on top of the continuous non-resonant background. This observation explains the experimental findings of Rudenko et al [12] and Maharjan et al [13] discussed in the introduction: The appearance of structures with highly-oscillatory angular distributions in the low ATI orders at peak laser intensities corresponding to $\gamma<1$ is consistent with the persistence of resonant contributions in the focal volume averaged spectra, which determines their pronounced manifestation both in the multiphoton and the tunnelling regimes.

5. Summary.

In summary, we have presented measurements of 2D photoelectron momentum spectra resulting from ATI of Xe and Ar in a wide range of wavelengths from 600 to 800 nm. The collected spectra recorded with an imaging spectrometer contain a large amount of information on the ionization process, where several mechanisms of different origin are involved. All experimental data have been carefully reproduced in the TDSE calculations. An analysis of the photoelectron spectra demonstrates the dominance of resonance-enhanced ionization in the considered wavelength range. The intermediate Rydberg states involved in the ionization have been reliably assigned based on the information extracted from the energy and angular distributions of the resonantly ionized electrons. Continuous variation of the laser wavelength allowed measuring a smooth evolution of the properties of the ATI photoelectron spectra as a function of the laser wavelength, where a number of consecutive channel-switching effects could be identified. We have shown that the appearance of the resonant sub-structure in the electron energy spectra may be influenced by the presence of the non-resonant contribution. At relatively low laser intensity we have observed a coherent addition of resonant and non-resonant ionization processes. Due to the absence of an intensity dependence in resonance-enhanced ionization, the presence of Freeman resonances can be easily observed both in the multiphoton and in the tunnelling regimes.

Acknowledgement

This work is part of the research program of the "Stichting voor Fundamenteel Onderzoek der Materie" (FOM), which is financially supported by the "Nederlandse Organisatie voor Wetenschappelijk Onderzoek" (NWO). KJS is supported by National Science Foundation Grant No. PHY-0701372 and the Ball Professorship at LSU.

References

[1] Agostini P, Fabre F, Mainfray G, Petite G, and Rahman N 1979 Free-Free Transitions Following Six-Photon Ionization of Xenon Atoms *Phys. Rev. Lett.* **42** 1127

[2] Bucksbaum P H, Freeman R R, Bashkansky M, and McIlrath T J 1987 Role of the ponderomotive potential in above-threshold ionization *J. Opt. Soc. Am. B* **4** 760

[3] Freeman R R, Bucksbaum P H, Milchberg H, Darack S, Schumacher D, and Geusic M 1987 Above-Threshold Ionization with Subpicosecond Laser Pulses *Phys. Rev. Lett.* **59** 1092

[4] Schyja V, Lang T and Helm H 1998 Channel switching in above-threshold ionization of xenon *Phys. Rev. A* **57** 3692

[5] Helm H, Bjerre N, Dyer M J, Huestis D L and Saeed M 1993 Images of photoelectrons formed in intense laser fields *Phys. Rev. Lett.* **70** 3221

[6] Helm H and Dyer M J 1994 Resonant and nonresonant multiphoton ionization of helium *Phys. Rev. A* **49** 2726

[7] Hansch P, Walker M A, Van Woerkom L D 1998 Eight- and nine-photon resonances in multiphoton ionization of xenon *Phys. Rev. A* **57** R709

[8] Schyja V, Lang T and Helm H 1996 in *Ultrafast Processes in Spectroscopy*, edited by Swelto et al. (Plenum Press, New York), p. 311

[9] Wiehle R, Witzel B, Helm H, Cormier E 2003 Dynamics of strong-field above-threshold ionization of argon: Comparison between experiment and theory *Phys. Rev. A* **67** 063405

[10] Rottke H, Wolff B, Tapernon M, Welge K H, and Feldmann D 1990 Resonant multiphoton ionization of xenon in intense sub-ps-laser pulses *Z. Phys. D* **15** 133

[11] Kaminski O**,** Wiehle R**,** Renard V, Kazmierczak A, Lavorel B, Faucher O, and Witzel B 2004 Wavelength dependence of multiphoton ionization of xenon *Phys. Rev. A* **70** 053413

[12] Rudenko A**,** Zrost K**,** Schröter C D**,** de Jesus V L B**,** Feuerstein B, Moshammer R and Ullrich J 2004 Resonant structures in the low-energy electron continuum for single ionization of atoms in the tunnelling regime *J. Phys.* B **37** L407

[13] Maharjan C M, Alnaser A S, Litvinyuk I, Ranitovic P and Cocke C L 2006 Wavelength dependence of momentum-space images of low-energy electrons generated by short intense laser pulses at high intensities *J. Phys.* B **39** 1955

[14] Ivanov I A and Kheifets A S 2009 Above-threshold-ionization structures in photoelectron momentum distributions for single ionization of He by a strong electromagnetic field *Phys. Rev.* A **80** 063418

[15] Potvliege R M, Mese E and Vučić S 2010 Multiphoton ionization and multiphoton resonances in the tunneling regime *Phys . Rev.* A **81** 053402

[16] Eppink A T J and Parker D H 1997 Velocity map imaging of ions and electrons using electrostatic lenses: Application in photoelectron and photofragment ion imaging of molecular oxygen *Rev. Sci. Instrum.* **68** 3477

[17] Vrakking M J J 2001 An iterative procedure for the inversion of two-dimensional ion/photoelectron imaging experiments *Rev. Sci. Instrum.* **72** 4084

[18] Kulander K C, Schafer K J and Krause J L 1992 *Atoms in Intense Laser Fields,* ed M Gavrila (New York: Academic Press)

[19] Schafer K J and Kulander K C 1990 Energy analysis of time-dependent wave functions: application to above-threshold ionization *Phys. Rev.* A **42** 5794

[20] Schafer K J 2008 Numerical methods in strong field physics, in *Strong Field Laser Physics*, ed T Brabec (New York: Springer Science + Business Media)

[21] Kulander K C and Rescigno T N 1991 Effective potentials for time-dependent calculations of multiphoton processes in atoms *Comput. Phys. Commun.* **63** 523

[22] Muller H G 1999 An efficient propagation scheme for the time-dependent Schrödinger equation in the velocity gauge *Laser Phys.* **9** 138

[23] Muller H G and Kooiman F C 1998 Bunching and focusing of tunneling wave packets in enhancement of high-order ATI *Phys. Rev. Lett.* **81** 1207

[24] Augst S, Meyerhofer D D, Strickland D and Chin S L 1991 Laser ionization of noble gases by Coulomb-barrier suppression *J. Opt. Soc. Am.* B **8** 858

[25] Marchenko T, Muller H G, Schafer K J and Vrakking M J J 2010 Electron angular distributions in near-threshold atomic ionization *J. Phys. B: At. Mol. Opt. Phys.* **43** 095601

[26] Huismans Y, Rouzée A, Gijsbertsen A, Logman P, Lépine F, Cauchy C, Zamith S, Marchenko T, Bakker J, Berden G, Redlich B, van der Meer L, Schafer K J and Vrakking M J J, manuscript in preparation

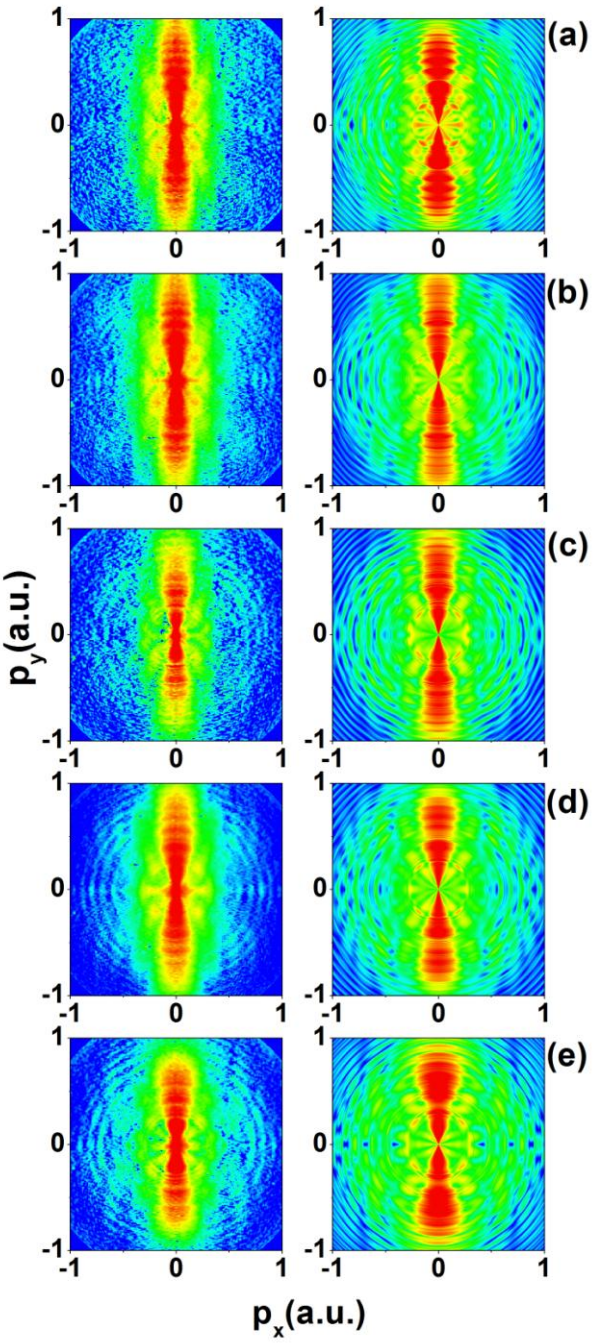


Figure 1. (Colour online) Experimental (left column) and calculated (right column) momentum maps for ionization of Ar at various wavelengths and intensities (from top to bottom): (a) 800 nm, A_{max}=0.85 a. u., 0.82×10^{14} W/cm^2; (b) 750 nm, A_{max}=0.98 a. u., 1.25×10^{14} W/cm^2; (c) 700 nm, A_{max}=0.88 a. u., 1.15×10^{14} W/cm^2; (d) 650 nm, A_{max}=0.93 a. u., 1.48×10^{14} W/cm^2; (e) 600 nm, A_{max}=0.78 a. u., 1.23×10^{14} W/cm^2. The logarithmic false-colour scale covers three orders of magnitude.

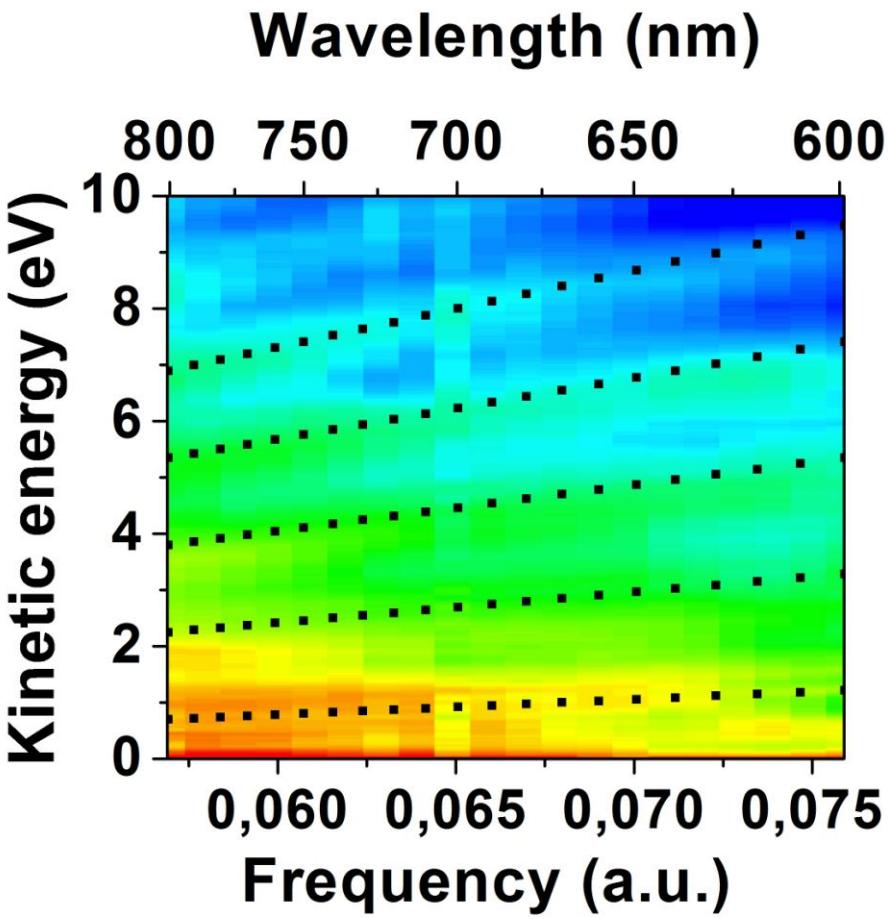


Figure 2. (Colour online) Experimental photoelectron spectra for ionization of Ar, shown as a function of laser wavelength. The spectra were normalised and angle-integrated. The logarithmic false-colour scale covers one order of magnitude. Dotted lines are calculated according to Eqn. (3), where E_b= -0.85 eV and n varies from 1 to 5, indicating low-order ionization processes involving the population of intermediate resonant states. The contour plot contains no sign of branches that could be attributed to high-order non-resonant processes given by Eqn. (1).

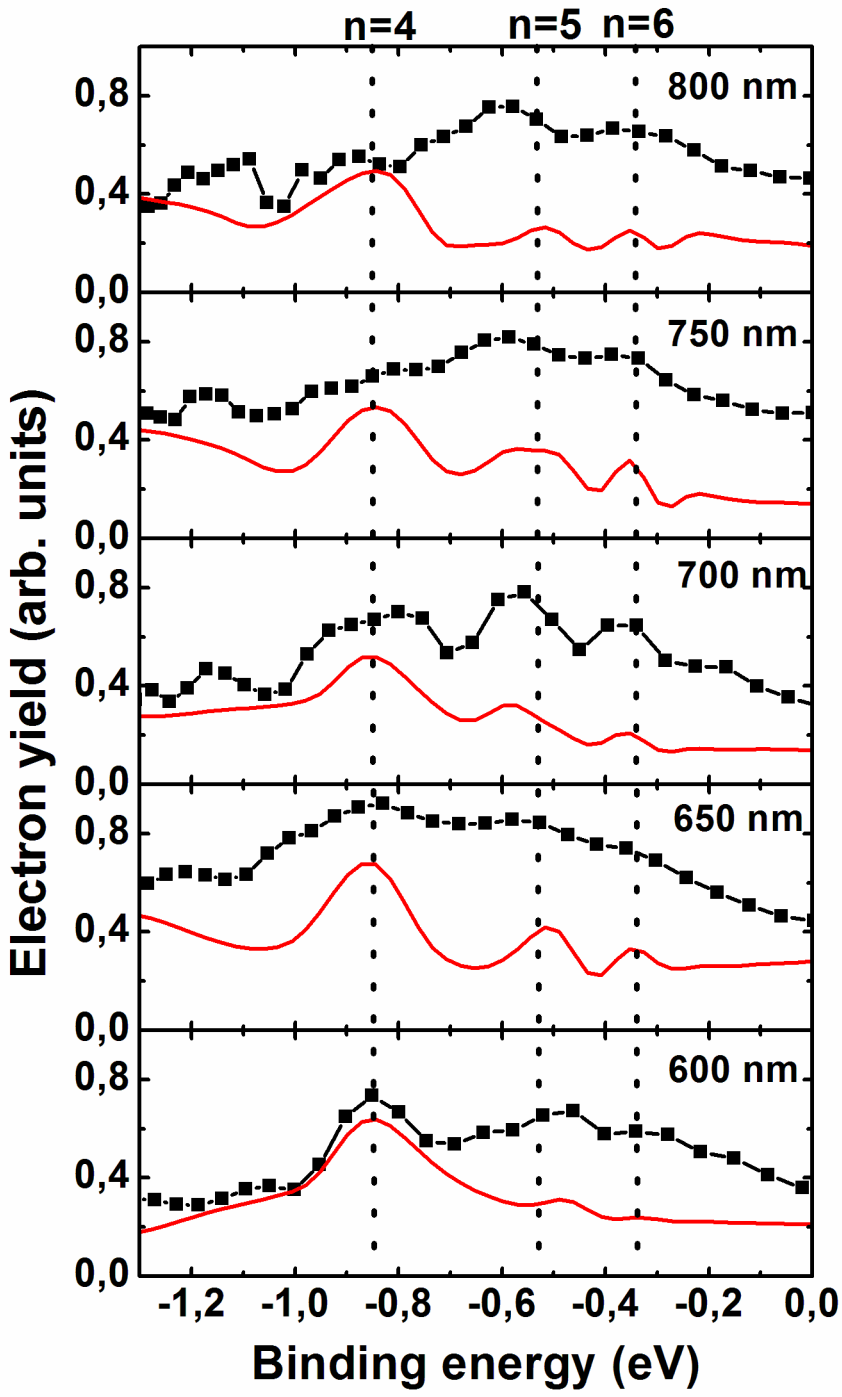


Figure 3. Experimental (squares) and calculated (solid line) photoelectron spectra for ionization of Ar at various wavelengths as indicated on the graphs. The photoelectron spectra are normalised, integrated over polar angles beyond ±25 degrees from the polarisation axis and downshifted by the energy of one photon. Dotted lines mark binding energies of Rydberg states with high orbital quantum number l and principal quantum number n=4, 5 and 6.

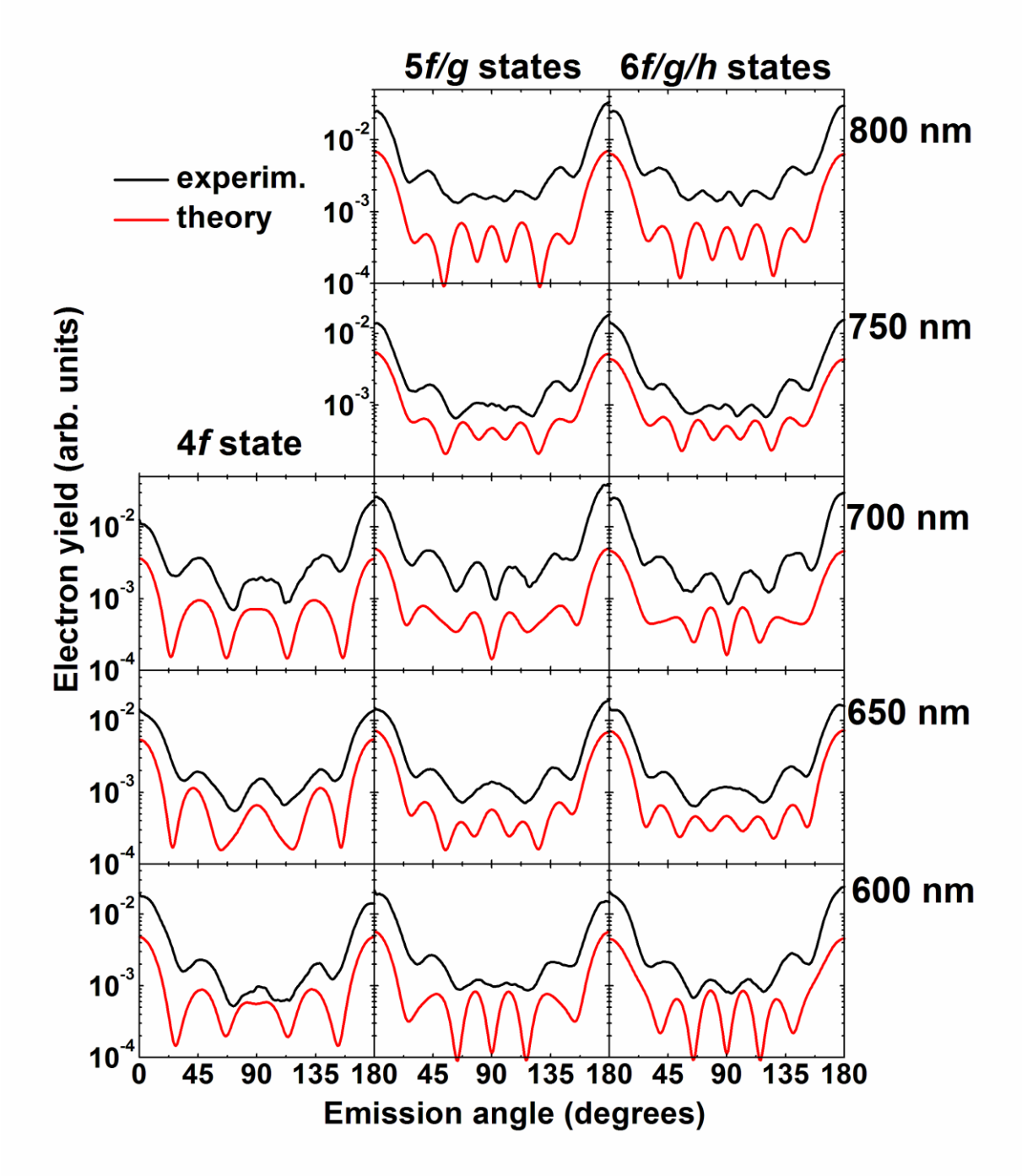


Figure 4. Experimental and calculated photoelectron angular distributions evaluated at photoelectron kinetic energies corresponding to one-photon ionization of Ar via 4*f*, 5*f*/*g* and 6*f*/*g*/*h* resonant states.

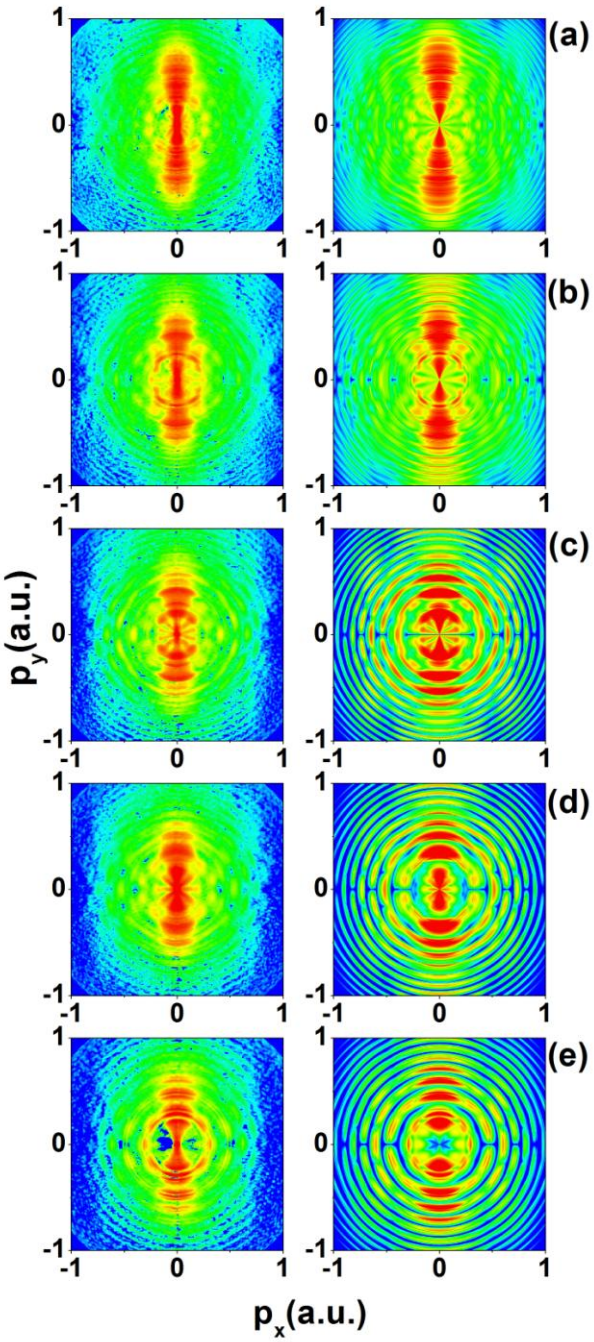


Figure 5. (Colour online) Experimental (left column) and calculated (right column) momentum maps for ionization of Xe at various wavelengths and intensities (from top to bottom): (a) 800 nm, A_{max}=0.77 a.u., 6.7×10^{13} W/cm^2; (b) 740 nm, A_{max}=0.7 a.u., 6.4×10^{13} W/cm^2; (c) 700 nm, A_{max}=0.55 a.u., 4.5×10^{13} W/cm^2; (d) 650 nm, A_{max}=0.52 a.u., 4.6×10^{13} W/cm^2; (e) 600 nm, A_{max}=0.53 a. u., 5.7×10^{13} W/cm^2. The logarithmic false-colour scale covers four orders of magnitude.

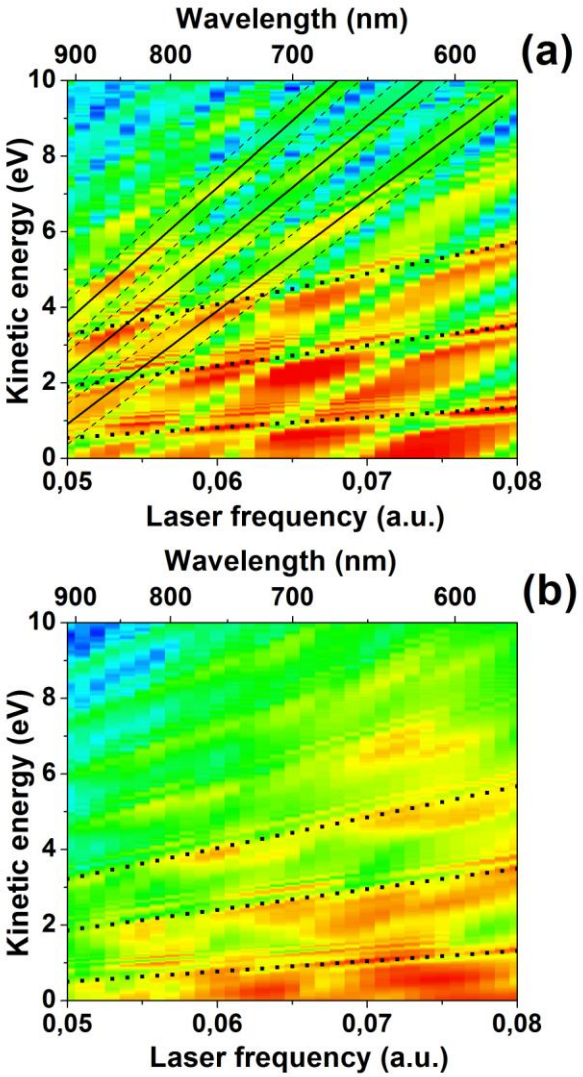


Figure 6. (Colour online) Calculated photoelectron spectra for ionization of Xe shown as a function of laser wavelength at (a) A_{max}=0.6 a.u., γ=1.57 and (b) A_{max}=0.9 a. u., γ=1.05. The photoelectron spectra are integrated over the laser focus volume and over all polar angles, and are arbitrarily divided by ω^{10} in order to enhance visibility of the spectra at the low-frequency edge. The logarithmic false-colour scale covers three and two orders of magnitude in (a) and (b), respectively. The branches observable in the contour plots are fitted according to Eqns. (1) and (3) with slopes corresponding to high-order (n=11, 12, 13 photons, solid lines) and low-order (n=1, 2, 3 photons, dotted lines) ionization processes for non-resonant and resonant ionization, respectively. The position and the widths of non-resonant branches in (a) are determined, respectively, by the effective intensity, corresponding to A_{eff} = 0.53 a.u. (solid lines) and by a range of intensities in the focal volume, corresponding to $0.45<A<A_{max}<0.6$ a.u. (dashed lines).